



Simultaneous temperature and pressure sensing based on a single optical resonator

YANRAN WU,^{1,2,†} BING DUAN,^{1,2,†} JIEN SONG,³ HUIPING TIAN,^{1,2}
JIN-HUI CHEN,^{4,6}  DAQUAN YANG,^{1,2,*}  AND SHANGUO HUANG^{1,5}

¹State Key Laboratory of Information Photonics and Optical Communications, Beijing University of Posts and Telecommunications, Beijing 100876, China

²School of Information and Communication Engineering, Beijing University of Posts and Telecommunications, Beijing 100876, China

³Jiangsu Shenyan Marine Information Technology and Equipment Innovation Center Co., Ltd, Suzhou 215000, China

⁴School of Electromagnetics and Acoustics, Xiamen University, Xiamen 361005, China

⁵School of Electronic Engineering, Beijing University of Posts and Telecommunications, Beijing 100876, China

⁶jimchen@xmu.edu.cn

[†]These authors contributed equally to this paper

*ydq@bupt.edu.cn

Abstract: We propose a dual-parameter sensor for the simultaneous detection of temperature and pressure based on a single packaged microbubble resonator (PMBR). The ultrahigh-quality ($\sim 10^7$) PMBR sensor exhibits long-term stability with the maximum wavelength shift about 0.2056 pm. Here, two resonant modes with different sensing performance are selected to implement the parallel detection of temperature and pressure. The temperature and pressure sensitivities of resonant Mode-1 are -10.59 pm/°C and 0.1059 pm/kPa, while the sensitivities of Mode-2 are -7.69 pm/°C and 0.1250 pm/kPa, respectively. By adopting a sensing matrix, the two parameters are precisely decoupled and the root mean square error of measurement are ~ 0.12 °C and ~ 6.48 kPa, respectively. This work promises the potential for the multi-parameters sensing in a single optical device.

© 2023 Optica Publishing Group under the terms of the [Optica Open Access Publishing Agreement](#)

1. Introduction

Optical sensing technologies play significant roles in the fields of environmental monitoring, biological sensing, and medical diagnostics due to the label free, anti-electromagnetic interference, multiplexing and remote sensing capabilities [1–6]. In particular, the high quality (Q) factor optical microresonators have been considered as promising platforms in optical detection by virtue of the exceptional sensitivity, small footprint and fast response [7–12]. This is mainly due to the fact that light can circulate millions of times in an ultra-high Q -factor optical microresonator, which significantly enhances the light-matter interaction and thus leads to the prominent improvement of sensitivity [13–17]. Moreover, the ultrahigh Q -factor of the resonator determines a narrow linewidth of the spectrum, enabling the detection of tiny variations, and thereby improving the detection limit [18–23]. Optical microresonators have been widely used in recent years for the detection of individual nanoparticle, biomolecular, and physical parameters [24–30]. Nevertheless, for practical applications, there are usually multiple effects in the optical detection, which is challenging to differentiate various sensing parameters in the conventional single-mode sensing scheme. For example, in the detection of nanoparticle, the sensing signal is synergistically determined by multiple parameters, such as the size, orientation, and polarizability [31].

The optical microresonator arrays based on wavelength division multiplexing technology provide multi-dimensional information, which enable the simultaneous detection of multiple parameters. For the past few years, several effective techniques based on sensor arrays have been developed for multi-parameters measurement [32–35]. Gao *et al.* innovatively proposed a dual-parameter sensor for the simultaneous measurement refractive index and flow rate by using an anti-resonant reflecting guidance [36]. Liu *et al.* achieved the detection of refractive index and temperature simultaneously based on the cascaded photonic crystal nanobeam cavities [37]. Mallik *et al.* realized the detection of ammonia vapor concentration and relative humidity by using two cascaded functionalized microsphere cavities [38]. However, the sensor arrays usually show the complex structure, sophisticate fabrication, and high detection consumption. Recently, there is emerging interest in a single multimode optical microresonator, exhibiting synthetic mode dimensions to different targets detection, which provides great opportunities for multi-parameter sensing in a single platform. In the previous work, we have achieved the precise decoupling of refractive index and temperature in the transition dynamics of a phase-change material by simultaneously monitoring two selected modes [39].

In this paper, we demonstrate the simultaneous measurement of temperature and pressure in a single packaged microbubble resonator (PMBR) with Q -factor of $\sim 1.4 \times 10^7$. Empowered by the two-parameters sensing matrix, the decoupling and parallel detection of multiple parameters can be implemented by selecting two resonant modes with different responses. The temperature sensitivities of Mode-1 and Mode-2 are $-10.59 \text{ pm}/^\circ\text{C}$ and $-7.69 \text{ pm}/^\circ\text{C}$, respectively, while the corresponding pressure sensitivities are $0.1059 \text{ pm}/\text{kPa}$ and $0.1250 \text{ pm}/\text{kPa}$. The obtained four sensitivities parameters can form a second-order full-rank sensitivity matrix. By applying a sensing matrix, the dual sensing parameters are decoupled with root mean square error of $\sim 0.12^\circ\text{C}$ and $\sim 6.48 \text{ kPa}$. This work combines optical microcavities detection with sensing matrix, which enables the independent measurement of multiple parameters.

2. Experimental setup and characterization

In Fig. 1(a), the experimental setup is shown in the left panel, a photograph of packaged microbubble-taper coupling system is photographed in the middle panel, and an optical microscope image of a microbubble resonator is shown in the right panel. The as-fabricated PMBR has a diameter of about $84 \mu\text{m}$ and a wall thickness of about $2 \mu\text{m}$, and the coupling microfiber diameter is about $1.7 \mu\text{m}$. The high Q -factor microbubble resonators are chosen as the sensing platform [40–42], which exhibits a hollow spherical section with large radial expansion size in comparison to these cylindrical ones of the overall device. From the perspective of electromagnetics, the extensive curvature of the microbubble resonator around the equatorial plane enhances the light limitation along the polar direction, guaranteeing a high Q -factor [43]. Meanwhile, the microbubble resonator has a natural microfluidic channel in the structure, and its light field can be distributed inside to enhance the interaction between light and the internal analytes to be measured and improve the sensing performance. The microbubble resonators are fabricated via heating and expanding process [44,45]. Firstly, the outer diameter hollow silica capillary is tapered to $\sim 30 \mu\text{m}$ with a hydrogen flame. Then, a syringe is used to pressurize the tapering capillary. Finally, the microbubble cavity is formed by heating the pressurized capillary using a CO_2 laser. The tapered fiber used for coupling is fabricated by “heating and pull” method using a hydrogen flame. By using micro/nano positioning stages, the relative position of the tapered fiber and microbubble is adjusted precisely. The microbubble-microfiber structure is embedded in a low refractive index polymer (MY-133, MY Polymers Ltd) to protect the device from environmental pollutants along with long-term coupling stability [46]. It is worth mentioning that the polymer has less absorption loss at 780 nm , which is able to guarantee a higher Q -factor.

In the experiment, a tunable laser at $\sim 780 \text{ nm}$ is evanescent coupled to the microbubble through the tapered fiber, thereby exciting resonant modes. The input laser power is kept as small

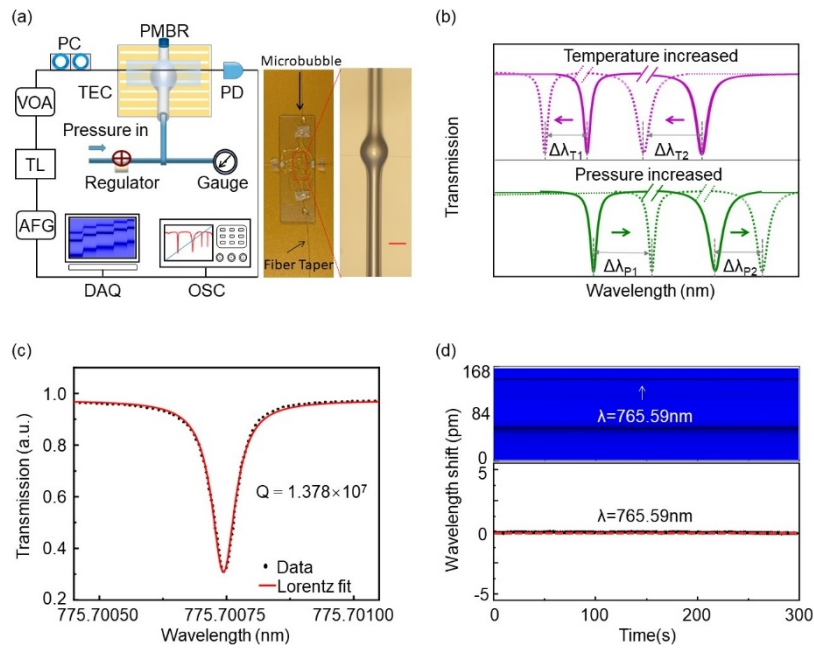


Fig. 1. (a) Experimental setup for dual-parameter sensing (left panel). PC: polarization controller, VOA: variable optical attenuator, PD: photodetector, DAQ: data acquisition card, OSC: oscilloscope, AFG: arbitrary function generator, TEC: temperature controller; Photograph of packaged microbubble-taper coupling system (middle panel); Optical microscope image of microbubble (right panel); Scale bar is 50 μm . (b) Schematic of multi-parameters sensing method. (c) Typical transmission spectrum of a resonant mode in a packaged microbubble resonator (PMBR). (d) Real-time acquisition of spectra (top) and the long-time stability of PMBR at room temperature (bottom). The maximum wavelength shift is about 0.2056 pm.

as 9.5 μW to avoid opto-thermal effect, and the insertion loss is $\sim 0.9 \text{ dB}$. Here, the polarization controller and variable optical attenuator are employed to tune the polarization state and light intensity, respectively. The transmission spectrum is collected by a photodetector, monitored by an oscilloscope, and recorded in real time by a data acquisition card. For pressure sensing, one port of the PMBR is connected with the pressure regulator and pressure gauge, and the other is sealed with ultraviolet glue. The applied pressure to the PMBR is controlled by a pressure regulator, and the pressure gauge is used for reference measurement. Figure 1(b) illustrates the schematic of dual parameters, i.e., temperature and pressure, sensing method, which is based on the variant sensing performance of two resonant modes. The ultrahigh Q -factor of 1.378×10^7 enables the high-resolution sensing as shown in Fig. 1(c). Considering that our sensor is close to the state of critical coupling, the intrinsic Q is about 2.8×10^7 . To assess the long-term stability of the sensing system, we measure the resonant wavelength shift over a period of time at room temperature. As shown in Fig. 1(d), the maximum wavelength shift of $\sim 0.2056 \text{ pm}$ is obtained within ~ 5 minutes, demonstrating the superior stability.

3. Pressure and temperature sensing experiments

3.1. Numerical simulation

To verify the feasibility of the proposed multiple parameters sensing in a single PMBR sensor, we simulated the geometry of the microbubble cavity using a rotational axisymmetric model in

two-dimensional COMSOL, and theoretically calculated the temperature and pressure sensitivity. Figure 2(a) shows a simulation of the optical intensity profile of resonant Mode-1 and Mode-2, and the insets are their corresponding optical mode-field distributions in PMBR. The calculated spectral shift correlating to the temperature change is plotted in Fig. 2(b), where the temperature sensitivity is calculated as [44]:

$$\frac{d\lambda}{dT} = \left(\frac{\partial\lambda}{\partial n_s} \sigma_s + \frac{\partial\lambda}{\partial n_p} \sigma_p \right) \quad (1)$$

where $\sigma_s = 1.1 \times 10^{-5}/^\circ\text{C}$, $\sigma_p = -3 \times 10^{-4}/^\circ\text{C}$ are thermo-optic coefficients of silica and polymer, respectively. For the thermal response of PMBR, the resonant wavelength shift is mainly caused by the thermo-optic effect of silica and encapsulating polymer, both of which should be considered for the influence on temperature. In Eq. (1), the coefficients $\frac{\partial\lambda}{\partial n_s}$ for Mode-1 and Mode-2 are 602 nm/RIU and 600 nm/RIU, while the coefficients $\frac{\partial\lambda}{\partial n_p}$ for Mode-1 and Mode-2 are 40 nm/RIU and 60 nm/RIU. Consequently, the temperature sensitivities S_{T1} and S_{T2} are -11.40 pm/ $^\circ\text{C}$ and -5.42 pm/ $^\circ\text{C}$ are derived for the two resonant modes. The variant sensing performance can be used to differentiate the thermal effect for dual-parameter sensors.

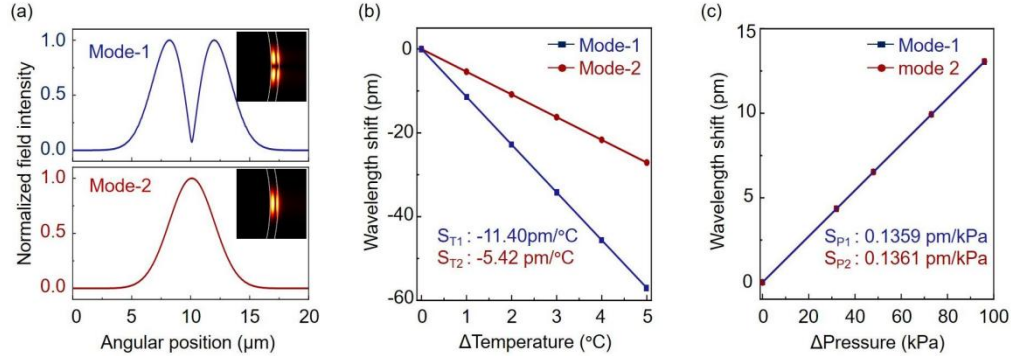


Fig. 2. (a) Angular field distributions of resonant Mode-1 (blue curve) and Mode-2 (red curve). Inset: Simulated optical field distribution of resonant modes in PMBR. (b) Calculated resonant wavelength shift of Mode-1 and Mode-2 related to the temperature. (c) Calculated resonant wavelength shift with applied pressure of Mode-1 and Mode-2.

As for the pressure sensing calculation, the stress-induced changes in the refractive index and strain-induced geometrical changes are considered, and the resonance wavelengths exhibit a red shift as the pressure increases [47]:

$$\frac{d\lambda}{\lambda} = \frac{dR}{R} + \frac{dn}{n} \quad (2)$$

$$\frac{dR}{R} = \frac{(4G + 3K)p_i r^3 - 4Gp_0 R^3 - 3Kp_0 r^3}{12GK(R^3 - r^3)} \quad (3)$$

$$\frac{dn}{n} = \frac{3(p_i r^3 - p_0 R^3)C}{n_{\text{eff}}(R^3 - r^3)} \quad (4)$$

where R and r are the outer and inner radius of a microbubble resonator, p_i and p_0 are the external and internal pressure, n_{eff} is the effective refractive index of resonant mode; the elastic-optic constant, shear and bulk modulus of silica are $C = 4 \times 10^{-12} \text{ m}^2/\text{N}$, $G = 31 \times 10^9 \text{ Pa}$ and

$K = 41 \times 10^9$ Pa, respectively. When the external pressure is a standard atmosphere, the pressure sensitivity of PMBR can be further represented as [47]:

$$\frac{d\lambda}{dP} = \lambda \left(\frac{3C}{n_{\text{eff}}} + \frac{4G + 3K}{12GK} \right) \frac{r^3}{(R^3 - r^3)} \quad (5)$$

We employ the finite element method to determine the coefficients of formula (5). Specifically, we set the following parameters: $\lambda = 776$ nm, $R = 43.9$ μm , $r = 42$ μm . When applying the pressure to PMBR, the stress field distributions of the polymer and the cavity wall is differed by 5 orders of magnitude, and therefore the stress effect of polymer is neglected. The two pressure sensitivities of $S_{P1} = 0.1359$ pm/kPa and $S_{P2} = 0.1361$ pm/kPa are obtained, as shown in Fig. 2(c).

3.2. Experimental results

Furthermore, the experiment is implemented by simultaneously monitoring two resonant modes. Note that there should be certain spectral intervals between the modes to ensure that they do not interfere with each other when disturbed by the external environment. Figure 3(a) shows the evolution of transmission spectra as the temperature increases by 1°C increments from 30°C to 35°C , while the internal relative pressure is kept at 0 kPa. The extracted wavelength shift on temperature is plotted in Fig. 3(b). The two temperature sensitivities S_{T1} and S_{T2} are -10.59 pm/ $^\circ\text{C}$ and -7.69 pm/ $^\circ\text{C}$. The synergistic effect of the negative thermo-optical effect of the polymer and the positive thermo-optical effect of the silica leads to a blue shift. Note that the extinction ratio of Mode-1 is changed considerably during the spectral shift, which is probably due to the adjacent mode coupling and the change of intrinsic mode loss. Figure 3(c) depicts the evolution of transmission spectra when the internal relative pressure increases from 0 kPa to 96 kPa, and the temperature is set as 30°C . The two pressure sensitivities S_{P1} and S_{P2} are 0.1059 pm/kPa and 0.1250 pm/kPa, as shown in Fig. 3(d). The resonant wavelength shows red-shift with increasing pressure, which is attributable to strain- and stress-induced geometrical variation and refractive index change [48]. The sensitivities of the two modes are used to construct the two-dimensional sensing matrix to achieve the decouple-measurement of the two parameters as discussed later. The two-dimensional sensing matrix has a relatively wide applicability to achieve decoupling of mode shifts in the same or opposite spectral shift for multi-parameter sensing [38]. Mathematically, the method is feasible when the sensing matrix is invertible. We also perform experimental verification of the wavelength shift in the same direction, as detailed in Appendix. Note that in our experiments, we mainly implement the high-order modes to realize high loaded Q factor although the extinction ratio is reduced. The high Q factor can enhance the sensing resolution for its narrow spectral resonance. Theoretically, the extinction ratio can be increased by changing the microfiber coupler radius or the coupling distance.

To assess the dual parametric sensing performance, a sensitivity matrix $M_{T,P}$ is defined as follows:

$$M_{T,P} = \begin{bmatrix} S_{T1} & S_{P1} \\ S_{T2} & S_{P2} \end{bmatrix} \quad (6)$$

The wavelength shift of the two modes ($\Delta\lambda_1$ and $\Delta\lambda_2$) induced by temperature (ΔT) and pressure changes (ΔP) can be given by:

$$\begin{bmatrix} \Delta\lambda_1 \\ \Delta\lambda_2 \end{bmatrix} = M_{T,P} \begin{bmatrix} \Delta T \\ \Delta P \end{bmatrix} \quad (7)$$

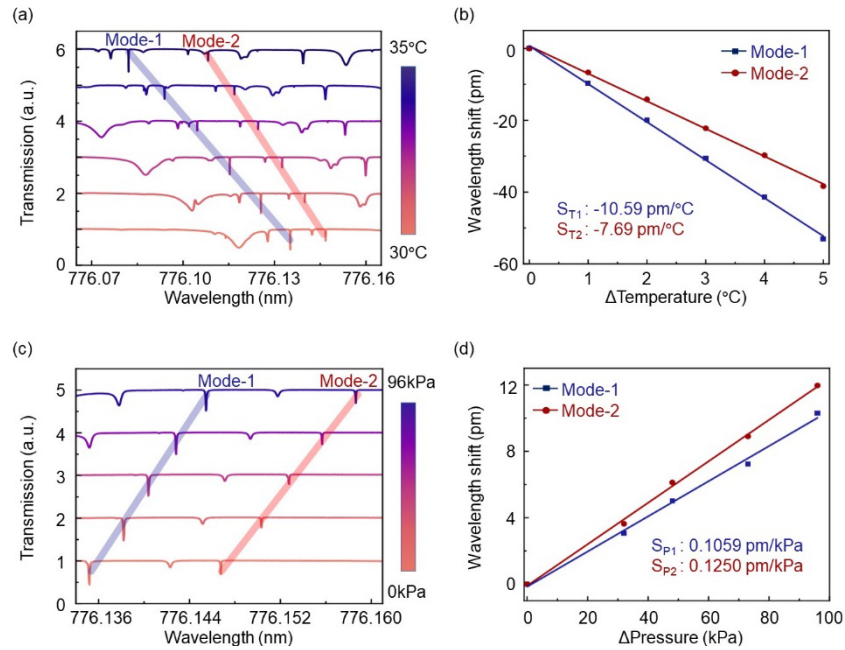


Fig. 3. (a) Transmission spectra of the PMBR change as the temperature increases from 30°C to 35°C in steps of 1°C. The curve is shifted for clarity. (b) Wavelength-temperature dependence of Mode-1 and Mode-2. (c) Evolution of transmission spectra of PMBR under different relative pressure variations (0 kPa, 32 kPa, 48 kPa, 73 kPa, and 96 kPa). The curve is shifted for clarity. (d) Wavelength-pressure dependence of Mode-1 and Mode-2.

Further, the variation of temperature and pressure can be solved by following matrix:

$$\begin{bmatrix} \Delta T \\ \Delta P \end{bmatrix} = M_{T,P}^{-1} \begin{bmatrix} \Delta \lambda_1 \\ \Delta \lambda_2 \end{bmatrix} \quad (8)$$

We investigate the temperature and pressure changes by concurrently observing the resonant wavelength shifts of Mode-1 and Mode-2. Herein, the initial state is given as 30°C and 0 kPa. The temperature changes from 30°C to 35°C, while the relative pressure changes from 0 kPa to 142 kPa. Figure 4(a) shows the evolution of transmission spectra when the temperature and pressure changes simultaneously, where the resonant wavelength changes of Mode-1 and Mode-2 can be obtained. By solving the inverse matrix equation in conjunction with Eq. (8), the dual parameters can be decoupled, as shown in Fig. 4(b-c). The derived root mean square error of the temperature and pressure are $\sim 0.12^{\circ}\text{C}$ and $\sim 6.48 \text{ kPa}$, respectively, showing reasonably good agreement. Table 1 gives a comparison of our proposed single microbubble sensor with related typical sensing schemes in terms of multi-parameters sensing performances. Compared with previous work, the single packaged microbubble resonator has the advantages of high sensing resolution and small footprint.

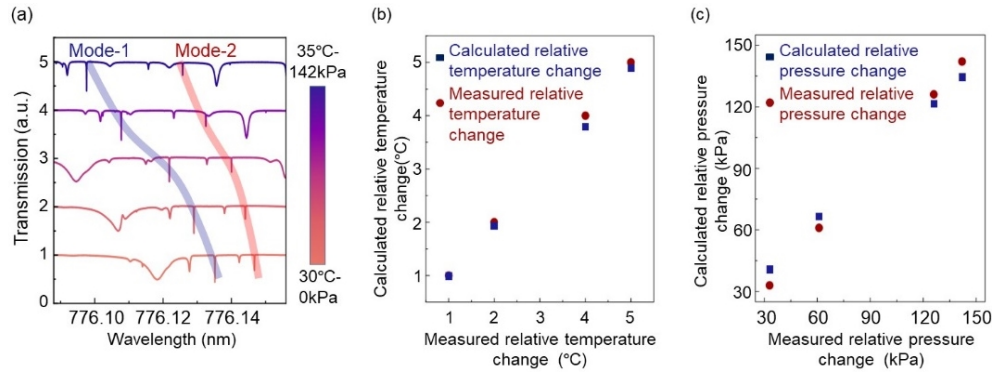


Fig. 4. (a) Evolution of transmission spectra of PMBR at different mixed temperature and pressure variations (0°C-0 kPa, 1°C-33 kPa, 2°C-61 kPa, 4°C-126 kPa, and 5°C-142 kPa). The curve is shifted for clarity. (b) Temperature comparison between calculated and measured data. (c) Pressure comparison between calculated and measured data.

Table 1. Comparison of typical sensing structures for multi-parameter sensing performance

Platform	Quality factor (Q)	Dimension	Measurement range	Resolution	Ref.
Fiber Bragg grating (FBG) + bending fiber	-	>9.5 mm (length)	1.3330-1.3785 RIU/ 25.4-95.4 °C	6.33×10^{-5} RIU /0.97 °C	[49]
FBG + nonadiabatic microfiber	-	> 10 mm (length)	0-18 mT/ 25-50 °C	-	[50]
Anti-resonant waveguide + bending fiber	-	> 6 mm (length)	1.3355-1.3758 RIU/ 25.4-85 °C	-	[51]
Fabry-Perot cavity + anti-resonant waveguide	-	>680 μ m (length)	121-541 °C/ 0-3.5 N	-	[52]
Cascade cylindrical microresonators	$\sim 10^4$	~ 20 μ m (diameter)	0-714 μ e/ 25-50 °C	-	[53]
Cascade microrings	$\sim 10^4$	~ 2 mm (diameter)	0-2.5%/ 22-28 °C	-	[54]
Cascade microspheres	$\sim 10^4$	~ 255 μ m (diameter)	40-69%RH/ 0.46-2.19 ppm	5.6×10^{-1} %RH /42 ppb	[38]
Microbubble	$\sim 10^7$	~ 84 μ m (diameter)	30-35 °C/ 0-142 kPa	0.003 °C/ 0.228 kPa	This work

4. Conclusion

In conclusion, we report a dual-parameter sensor based on a single PMBR for simultaneous temperature and pressure detection. The PMBR sensor exhibits long-time stability with a high Q -factor of $\sim 1.4 \times 10^7$. Two resonant modes with different responses are selected to simultaneously detect the pressure and temperature. For Mode-1, the temperature and pressure sensitivities are -10.59 pm/°C and 0.1059 pm/kPa, while those of Mode-2 are -7.69 pm/°C and 0.1250 pm/kPa, respectively. Furthermore, we verify the feasibility of parallel detection of temperature and pressure by applying a sensing matrix. With the simple fabrication method, the reported dual-parameter sensor can avoid the complex cascade operation, which exhibits the potential for the multi-parameters detection in a single sensing platform. Besides, dual-parameter

sensors also can be combined with other signal processing methods, such as machine learning, which facilitates the promotion of intelligent multi-parameter sensing application.

Appendix

In our previous experiments, the sensor is encapsulated using a polymer with a negative refractive index, resulting in a spectral blue-shift for temperature sensing. Thus, the wavelength shifts caused by increased temperature and pressure are in the opposite direction. In the supplemental experiments, the sensor is not encapsulated with a polymer, resulting in a spectral red-shift for temperature sensing, thus the wavelength shifts caused by the temperature and pressure variations are both in the same direction.

In experiments, two modes with a certain spectral separation are selected from the transmission spectrum, i.e., Mode-3 and Mode-4, respectively. Figure 5(a) shows the evolution of transmission spectra as the temperature increases by 1°C increments from 30°C to 33°C, while the internal relative pressure is kept at 0 kPa. The resonant wavelength shows red-shift with increasing temperature. The extracted wavelength shift on temperature is plotted in Fig. 5(b). The two temperature sensitivities S_{T3} and S_{T4} are 1.137 pm/°C and 1.471 pm/°C. Figure 5(c) depicts the evolution of transmission spectra when the internal relative pressure increases from 0 kPa to 71 kPa, and the temperature is set as 30°C. The two pressure sensitivities S_{P3} and S_{P4} are 0.1723 pm/kPa and 0.1692 pm/kPa, as shown in Fig. 5(d).

We investigate the temperature and pressure variations by concurrently observing the resonant wavelength shifts of Mode-3 and Mode-4. Herein, the initial state is given as 30°C and 0 kPa. The temperature changes from 30°C to 33°C, while the relative pressure changes from 0 kPa

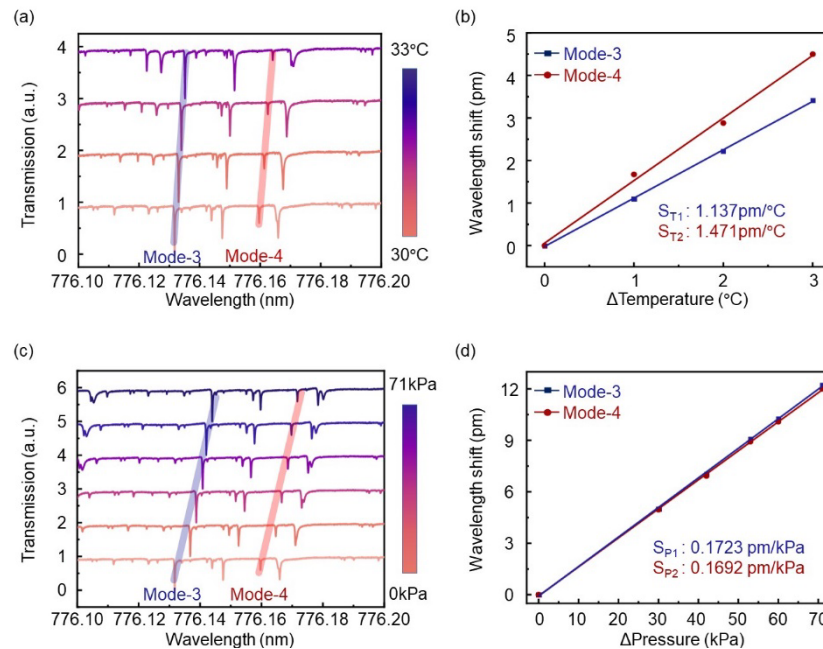


Fig. 5. (a) Transmission spectra of the PMBR change as the temperature increases from 30°C to 33°C in steps of 1°C. The curve is shifted for clarity. (b) Wavelength-temperature dependence of Mode-3 and Mode-4. (c) Evolution of transmission spectra of PMBR under different relative pressure variations (0 kPa, 30 kPa, 42 kPa, 53 kPa, 60 kPa, and 71 kPa). The curve is shifted for clarity. (d) Wavelength-pressure dependence of Mode-3 and Mode-4.

to 52 kPa. Figure 6(a) shows the evolution of transmission spectra when the temperature and pressure changes simultaneously, where the resonant wavelength changes of Mode-3 and Mode-4 can be obtained. By solving the inverse matrix equation in conjunction with Eq. (8), the dual parameters can be decoupled, as shown in Fig. 6(b-c). The derived root mean square error of the temperature and pressure are $\sim 0.13^\circ\text{C}$ and ~ 2.02 kPa, respectively. This demonstrates that wavelength shifts in the same direction within a sensor can also be decoupled.

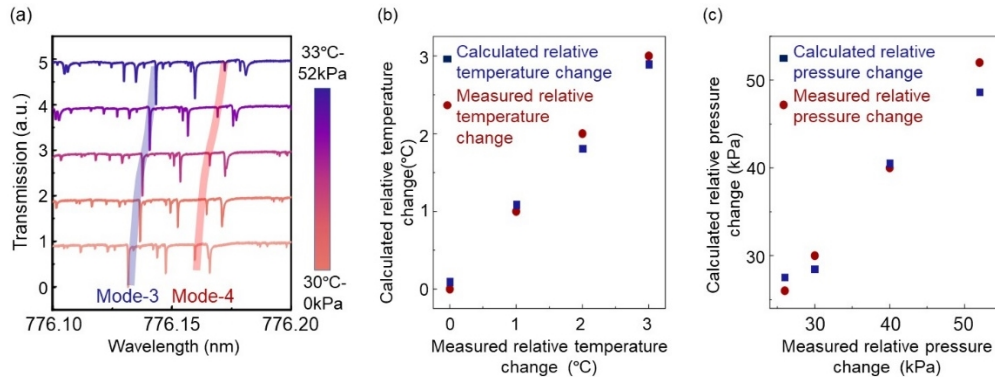


Fig. 6. (a) Evolution of transmission spectra of PMBR at different mixed temperature and pressure variations (0°C -0 kPa, 0°C -30 kPa, 1°C -26 kPa, 2°C -40 kPa, and 3°C -52 kPa). The curve is shifted for clarity. (b) Temperature comparison between calculated and measured data. (c) Pressure comparison between calculated and measured data.

Funding. National Natural Science Foundation of China (11974058, 12274357, 62005231); Beijing Nova Program from Beijing Municipal Science and Technology Commission (Z201100006820125); Beijing Municipal Natural Science Foundation (Z210004); State Key Laboratory of Information Photonics and Optical Communications, BUPT, China (IPOC2021ZT01).

Acknowledgments. The authors thank Prof. Chuan Wang, Dr. Xiao-Chong Yu, Dr. Yongpan Gao and Dr. Shuing Tang for the helpful discussions.

Disclosures. The authors declare no conflicts of interest.

Data availability. Data underlying the results presented in this paper are not publicly available at this time but may be obtained from the authors upon reasonable request.

References

1. Y. F. Xiao and Q. H. Gong, "Optical microcavity: from fundamental physics to functional photonics devices," *Sci. Bull.* **61**(3), 185–186 (2016).
2. Y. Zhi, X.-C. Yu, Q. Gong, L. Yang, and Y.-F. Xiao, "Single nanoparticle detection using optical microcavities," *Adv. Mater.* **29**(12), 1604920 (2017).
3. X.-C. Yu, Y. Zhi, S.-J. Tang, B.-B. Li, Q. Gong, C.-W. Qiu, and Y.-F. Xiao, "Optically sizing single atmospheric particulates with a 10-nm resolution using a strong evanescent field," *Light: Sci. Appl.* **7**(4), 18003 (2018).
4. H. Ghali, H. Chibli, J. L. Nadeau, P. Bianucci, and Y.-A. Peter, "Real-time detection of staphylococcus aureus using whispering gallery mode optical microdisks," *Biosensors* **6**(2), 20 (2016).
5. K. Wang, Y. P. Gao, R. Jiao, and C. Wang, "Recent progress on optomagnetic coupling and optical manipulation based on cavity-optomagnonics," *Front. Phys.* **17**(4), 42201 (2022).
6. S. Wondimu, M. Hippler, C. Hussal, A. Hofmann, S. Krämmer, J. Lahann, H. Kalt, W. Freude, and C. Koos, "Robust label-free biosensing using microdisk laser arrays with on-chip references," *Opt. Express* **26**(3), 3161–3173 (2018).
7. J. Zhu, S. K. Ozdemir, Y.-F. Xiao, L. Li, L. He, D.-R. Chen, and L. Yang, "On-chip single nanoparticle detection and sizing by mode splitting in an ultrahigh-q microresonator," *Nat. Photonics* **4**(1), 46–49 (2010).
8. L. He, Ş. K. Özdemir, J. Zhu, W. Kim, and L. Yang, "Detecting single viruses and nanoparticles using whispering gallery microlasers," *Nat. Nanotechnol.* **6**(7), 428–432 (2011).
9. Q.-T. Cao, H. Wang, C.-H. Dong, H. Jing, R.-S. Liu, X. Chen, L. Ge, Q. Gong, and Y.-F. Xiao, "Experimental demonstration of spontaneous chirality in a nonlinear microresonator," *Phys. Rev. Lett.* **118**(3), 033901 (2017).
10. J.-H. Chen, X. Shen, S.-J. Tang, Q.-T. Cao, Q. Gong, and Y.-F. Xiao, "Microcavity nonlinear optics with an organically functionalized surface," *Phys. Rev. Lett.* **123**(17), 173902 (2019).

11. L. Zhang, Y. Tang, and L. Tong, "Micro-/nanofiber optics: Merging photonics and material science on nanoscale for advanced sensing technology," *iScience* **23**(1), 100810 (2020).
12. S. Frustaci and F. Vollmer, "Whispering-gallery mode (WGM) sensors: review of established and WGM-based techniques to study protein conformational dynamics," *Curr. Opin. Chem. Biol.* **51**, 66–73 (2019).
13. X. Zhang, Q.-T. Cao, Z. Wang, Y.-x. Liu, C.-W. Qiu, L. Yang, Q. Gong, and Y.-F. Xiao, "Symmetry-breaking-induced nonlinear optics at a microcavity surface," *Nat. Photonics* **13**(1), 21–24 (2019).
14. Y.-F. Xiao, C.-L. Zou, B.-B. Li, Y. Li, C.-H. Dong, Z.-F. Han, and Q. Gong, "High-q exterior whispering-gallery modes in a metal-coated microresonator," *Phys. Rev. Lett.* **105**(15), 153902 (2010).
15. Q. Ba, Y. Zhou, J. Li, W. Xiao, L. Ye, Y. Liu, J. H. Chen, and H. Chen, "Conformal optical black hole for cavity," *eLight* **2**(1), 19 (2022).
16. X. Jiang, A. J. Qavi, S. H. Huang, and L. Yang, "Whispering-gallery sensors," *Matter* **3**(2), 371–392 (2020).
17. M. R. Foreman, J. D. Swaim, and F. Vollmer, "Whispering gallery mode sensors," *Adv. Opt. Photonics* **7**(2), 168–240 (2015).
18. F. Vollmer, S. Arnold, and D. Keng, "Single virus detection from the reactive shift of a whispering-gallery mode," *Proc. Natl. Acad. Sci.* **105**(52), 20701–20704 (2008).
19. Y. Yin, Y. Niu, M. Ren, W. Wu, W. Zhao, J. Nan, Z. Zheng, Y. Zhang, and M. Ding, "Strain sensing based on a microbottle resonator with cleaned-up spectrum," *Opt. Lett.* **43**(19), 4715–4718 (2018).
20. J. Su, "Label-free biological and chemical sensing using whispering gallery mode optical resonators: past, present, and future," *Sensors* **17**(3), 540 (2017).
21. T. Wang, X.-F. Liu, Y. Hu, G. Qin, D. Ruan, and G.-L. Long, "Rapid and high precision measurement of opto-thermal relaxation with pump-probe method," *Sci. Bull.* **63**(5), 287–292 (2018).
22. Q. Song, "Emerging opportunities for ultra-high q whispering gallery mode microcavities," *Sci. China Phys. Mech. Astron.* **62**(7), 74231 (2019).
23. D. Yu, M. Humar, K. Meserve, R. C. Bailey, S. N. Chormaic, and F. Vollmer, "Whispering-gallery-mode sensors for biological and physical sensing," *Nat. Rev. Methods Primers* **1**(1), 83 (2021).
24. H. Jing, H. Lü, S. Özdemir, T. Carmon, and F. Nori, "Nanoparticle sensing with a spinning resonator," *Optica* **5**(11), 1424–1430 (2018).
25. Z. Guo, Q. Lu, C. Zhu, B. Wang, Y. Zhou, and X. Wu, "Ultra-sensitive biomolecular detection by external referencing optofluidic microbubble resonators," *Opt. Express* **27**(9), 12424–12435 (2019).
26. Y.-n. Zhang, T. Zhou, B. Han, A. Zhang, and Y. Zhao, "Optical bio-chemical sensors based on whispering gallery mode resonators," *Nanoscale* **10**(29), 13832–13856 (2018).
27. A. V. Saetchnikov, E. A. Tcherniavskaia, V. A. Saetchnikov, and A. Ostendorf, "Multiresonator imaging sensor for the aerial parameters detection," *IEEE J. Miniat. Air Space Syst.* **2**(2), 84–91 (2021).
28. J. Liao and L. Yang, "Optical whispering-gallery mode barcodes for high-precision and wide-range temperature measurements," *Light: Sci. Appl.* **10**(1), 32 (2021).
29. W. Liu, Y.-L. Chen, S.-J. Tang, F. Vollmer, and Y.-F. Xiao, "Nonlinear sensing with whispering-gallery mode microcavities: From label-free detection to spectral fingerprinting," *Nano Lett.* **21**(4), 1566–1575 (2021).
30. W. Liu, W. Li, R. Wang, E. Xing, N. Jing, Y. Zhou, J. Tang, and J. Liu, "Magnetic sensor based on WGM hollow microbubble resonator filled with magnetic fluid," *Opt. Commun.* **497**, 127148 (2021).
31. Y. Xu, S.-J. Tang, X.-C. Yu, Y.-L. Chen, D. Yang, Q. Gong, and Y.-F. Xiao, "Mode splitting induced by an arbitrarily shaped rayleigh scatterer in a whispering-gallery microcavity," *Phys. Rev. A* **97**(6), 063828 (2018).
32. P. Zhang, D. He, C. Zhang, and Z. Yan, "FDTD simulation: simultaneous measurement of the refractive index and the pressure using microdisk resonator with two whispering-gallery modes," *Sensors* **20**(14), 3955 (2020).
33. Z. Ding, P. Liu, J. Chen, D. Dai, and Y. Shi, "On-chip simultaneous sensing of humidity and temperature with a dual-polarization silicon microring resonator," *Opt. Express* **27**(20), 28649–28659 (2019).
34. L. Ye, X. Liu, D. Pei, J. Peng, S. Liu, K. Guo, X. Li, X. Chen, X. Zhang, and D. Yang, "Simultaneous detection of relative humidity and temperature based on silicon on-chip cascaded photonic crystal nanobeam cavities," *Crystals* **11**(12), 1559 (2021).
35. P. Liu and Y. Shi, "Simultaneous measurement of refractive index and temperature using a dual polarization ring," *Appl. Opt.* **55**(13), 3537–3541 (2016).
36. R. Gao, D. Lu, J. Cheng, and Z.-m. Qi, "Simultaneous measurement of refractive index and flow rate using graphene-coated optofluidic anti-resonant reflecting guidance," *Opt. Express* **25**(23), 28731–28742 (2017).
37. P. Liu and Y. Shi, "Simultaneous measurement of refractive index and temperature using cascaded side-coupled photonic crystal nanobeam cavities," *Opt. Express* **25**(23), 28398–28406 (2017).
38. A. K. Mallik, G. Farrell, M. Ramakrishnan, V. Kavungal, D. Liu, Q. Wu, and Y. Semenova, "Whispering gallery mode micro resonators for multi-parameter sensing applications," *Opt. Express* **26**(24), 31829–31838 (2018).
39. D.-Q. Yang, J.-h. Chen, Q.-T. Cao, B. Duan, H.-J. Chen, X.-C. Yu, and Y.-F. Xiao, "Operando monitoring transition dynamics of responsive polymer using optofluidic microcavities," *Light: Sci. Appl.* **10**(1), 128 (2021).
40. X. Xu, X. Jiang, G. Zhao, and L. Yang, "Phone-sized whispering-gallery microresonator sensing system," *Opt. Express* **24**(23), 25905–25910 (2016).
41. C. He, H. Sun, J. Mo, C. Yang, G. Feng, H. Zhou, and S. Zhou, "Temperature sensor based on high-q polymethyl-methacrylate optical microbubble," *Laser Phys.* **28**(7), 076202 (2018).

42. G. Wang, X. Liu, Z. Gui, Y. An, J. Gu, M. Zhang, L. Yan, G. Wang, and Z. Wang, "A high-sensitive pressure sensor using a single-mode fiber embedded microbubble with thin film characteristics," *Sensors* **17**(6), 1192 (2017).
43. A. Barucci, S. Berneschi, A. Giannetti, F. Baldini, A. Cosci, S. Pelli, D. Farnesi, G. C. Righini, S. Soria, and G. Nunzi Conti, "Optical microbubble resonators with high refractive index inner coating for bio-sensing applications: An analytical approach," *Sensors* **16**(12), 1992 (2016).
44. D. Yang, B. Duan, A. Wang, Y. Pan, C. Wang, Y. Ji, and J.-h. Chen, "Packaged microbubble resonator for versatile optical sensing," *J. Lightwave Technol.* **38**(16), 4555–4559 (2020).
45. D. Yang, A. Wang, J.-H. Chen, X.-C. Yu, C. Lan, Y. Ji, and Y.-F. Xiao, "Real-time monitoring of hydrogel phase transition in an ultrahigh q microbubble resonator," *Photonics Res.* **8**(4), 497–502 (2020).
46. G. C. Righini and S. Soria, "Biosensing by WGM microspherical resonators," *Sensors* **16**(6), 905 (2016).
47. Z. Chen, Z. Guo, X. Mu, Q. Li, X. Wu, and H. Fu, "Packaged microbubble resonator optofluidic flow rate sensor based on bernoulli effect," *Opt. Express* **27**(25), 36932–36940 (2019).
48. Y. Yang, S. Saurabh, J. M. Ward, and S. N. Chormaic, "High-q, ultrathin-walled microbubble resonator for aerostatic pressure sensing," *Opt. Express* **24**(1), 294–299 (2016).
49. Y. Chen, Q. Han, T. Liu, F. Liu, and Y. Yao, "Simultaneous measurement of refractive index and temperature using a cascaded FBG/droplet-like fiber structure," *IEEE Sensors J.* **15**(11), 6432–6436 (2015).
50. Y. Zhang, S. Pu, Y. Li, Z. Hao, D. Li, S. Yan, M. Yuan, and C. Zhang, "Magnetic field and temperature dual-parameter sensor based on nonadiabatic tapered microfiber cascaded with FBG," *IEEE Access* **10**, 15478–15486 (2022).
51. J. Zheng, B. Liu, L. Zhao, R. Ullah, Y. Mao, J. Ren, and T. Wang, "An optical sensor designed from cascaded anti-resonant reflection waveguide and fiber ring-shaped structure for simultaneous measurement of refractive index and temperature," *IEEE Photonics J.* **14**(4), 1–8 (2022).
52. J. Zheng, B. Liu, L. Zhao, R. Ullah, Y. Mao, J. Ren, and T. Wang, "Compact optical fiber sensor based on silica capillary tube for simultaneous high temperature and transverse load measurement," *IEEE Photonics J.* **14**(4), 1–8 (2022).
53. V. Kavungal, G. Farrell, Q. Wu, A. K. Mallik, C. Shen, and Y. Semenova, "Packaged inline cascaded optical micro-resonators for multi-parameter sensing," *Opt. Fiber Technol.* **50**, 50–54 (2019).
54. M. S. Kwon and W. H. Steier, "Microring-resonator-based sensor measuring both the concentration and temperature of a solution," *Opt. Express* **16**(13), 9372–9377 (2008).